Age-related Changes in Diffuse Optical Tomography Sensitivity by Source-Detector Separation in Infancy

Xiaoxue Fu [a], John E. Richards [a]

[a] Department of Psychology, University of South Carolina, United States

Corresponding author:

Xiaoxue Fu

Email address: xiaoxuef@mailbox.sc.edu

Abstract

Diffuse optical tomography (DOT) uses near-infrared light spectroscopy (NIRS) to measure changes in cerebral hemoglobin concentration. Anatomical interpretations of the location that generates the hemodynamic signal requires accurate descriptions of DOT sensitivity to the underlying cortical structures. Such information is limited for pediatric populations because they undergo rapid head and brain development. The present study used photon propagation simulation methods to examine DOT sensitivity profiles in realistic head models among infants ranging from 2 weeks to 24 months with narrow age bins, children (4 and 12 years) and adults (20 to 24 years). The sensitivity profile changed systematically with the source-detector separation distance. The peak of the sensitivity function was largest at the smallest separation distance and decreased as source-detector distance increased. The fluence value dissipated more quickly with penetration depth at the shorter source-detector separations than the longer separations. There were age-related differences in the shape and variance of DOT sensitivity profiles across a wide range of source-detector separations. Our findings have important implications in the design of sensor placement and DOT image reconstruction in NIRS and fNIRS research. Age-appropriate realistic head models should be used to provide anatomical guidance for standalone DOT data in infants.

Keywords:

Diffuse optical tomography, near-infrared light spectroscopy, Monte Carlo simulation, infant, development, head models

Introduction

Diffuse optical tomography (DOT) uses near-infrared light spectroscopy (NIRS) to measure changes in cerebral hemoglobin concentration (Huppert, Franceschini, & Boas, 2009). DOT does not provide anatomical information about the location of the hemodynamic signal. Determining the extent to which the DOT instrument can detect changes in cortical activities and the cortical region(s) it is sampling requires comprehensive understanding of the DOT sensitivity profile. Monte Carlo simulations are used to simulate the propagation of photons through head and brain tissues (Boas, Culver, Stott, & Dunn, 2002). The forward model can then guide DOT image reconstruction to recover the brain locations of hemoglobin concentration changes (Cooper et al., 2012; Culver, Siegel, Stott, & Boas, 2003). DOT sensitivity profiles have been studied in adults. However, There are considerable brain structural changes during infancy through childhood and adulthood (Richards & Conte, 2020; Richards & Xie, 2015). Accurate forward models depend on the use of realistic head models that accounts for age-related changes in the head (Brigadoi, Aljabar, Kuklisova-Murgasova, Arridge, & Cooper, 2014; Fukui, Ajichi, & Okada, 2003). The present study examined age-related changes in DOT sensitivity profiles. We used age-appropriate, realistic head models with extensive coverage of the infancy period (2 weeks through 2 years), two child ages (4, 12 years), and young adults (20 to 24 years).

The Use of Monte Carlo Simulations to Estimate DOT Sensitivity Profile

DOT sensitivity inside the head is often measured with Monte Carlo simulation methods that model the propagation of photons through heterogeneous tissue structures such as the human brain (Jacques & Wang, 1995). The inputs to Monte Carlo simulation are a segmented MRI that define tissue types, optical properties of the tissue types, simulated injection of light photons into the head, and an algorithm describing the path of the photon through the tissues. A computer

program is used that takes this information and simulates the path of injected photons through the head media (e.g., (tMCimg; Boas et al., 2002); (MCX; Fang & Boas, 2009a); (MMC; Fang, 2010); (MCML; Jacques & Wang, 1995; L. Wang, Jacques, & Zheng, 1995) ; (TOAST++; Schweiger & Arridge, 2014)).

The output from the Monte Carlo simulation program is a distribution of photon travel across the head, and DOT sensitivity can be quantified from Monte Carlo simulation outputs. The DOT sensitivity is conceptualized as the extent to which the detected signal is influenced by changes in optical properties in the given region of tissue (Mansouri, L'Huillier, Kashou, & Humeau, 2010). One representation of DOT sensitivity is the spatial sensitivity profile. The profiles depict the fluence distribution of detected photons (Boas et al., 2002). It can be quantified by the probability of a photon travelling from a source-electrode location to a voxel inside the head ("2-point Green's function"; Strangman, Li, & Zhang, 2013). A second approach to quantify DOT sensitivity is to use the photon measurement density function (PMDF). The PMDF quantifies optical sensitivity in NIRS source-detector recording by calculating the product of the fluence distribution at the source location and the detector location (PMDF; Brigadoi et al., 2014; Brigadoi & Cooper, 2015; or "3-point Green's function"; Strangman et al., 2013). We will call this the “Source-Detector Channel DOT” (S-D Channel DOT). S-D Channel DOT represents the probability that a photon injected from the source and measured at the detector location has propagated through a given tissue. DOT sensitivity is quantified as each location at which a photon traverses through a given tissue region, or “partial path length” (PPL; Mansouri et al., 2010; Strangman, Zhang, & Li, 2014; Wang, Ayaz, & Izzetoglu, 2019). PPL represent the penetration depths of the photon measured in the medium (Mansouri et al., 2010).

DOT Sensitivity Profile by Source-Detector Separation Distances

The DOT sensitivity changes as a function of source-detector separation distances (Mansouri et al., 2010; Strangman et al., 2013; Strangman et al., 2014; Wang et al., 2019). As the source-detector distance increases, the fluence distribution covers wider tissue regions, extends deeper into the brain, and decreases in DOT sensitivity. For example, it has been found that for 20 mm source-detector separation the fluence distribution was largely confined to shallow layers of the head model and about 6% of the total sensitivity was attributed to the brain (gray and white matters) (Strangman et al., 2013; Strangman et al., 2014). Sensitivity to the brain increased linearly from 20 mm up to 45 mm separation (Mansouri et al., 2010; Strangman et al., 2013; Strangman et al., 2014; Wang et al., 2019). The increase in sensitivity to the brain was less steep at larger distances (Strangman et al., 2013; Strangman et al., 2014). There was a trade-off between penetration depth and signal intensity. Signal intensity decreased monotonically and exponentially with increased depth at all separation distances (Strangman et al., 2013). Wang et al. (2019) showed that the signal strength was reduced as source-detector separation increased. Hence, the optimal separation distances for measuring brain activity need to be determined based on the consideration of depth sensitivity, the desired spatial resolution of the measurement regions, and the achievable signal strength for the measurement device.

It is important to use age-specific realistic head models for estimating DOT sensitivity. There is substantial increase in skull thickness (Emberson, Crosswhite, Goodwin, Berger, & Aslin, 2016), CSF volume (Makropoulos et al., 2016), and global gray matter / white matter growth (Gilmore et al., 2011; Makropoulos et al., 2016; Richards & Conte, 2020; Richards & Xie, 2015). There are indeed developmental effects in DOT sensitivity. Age was positively associated with the depth sensitivity in the frontal and occipital regions in head models of

children between 5 to 11 years old (Whiteman, Santosa, Chen, Perlman, & Huppert, 2017). Fukui et al. (2003) compared DOT sensitivity by separation distances in neonates (20-24 weeks) and adults. They found that the sensitivity to brain tissues was greater in neonates than adults across all separation distances (10 mm to 60 mm). Additionally, there was an age-by-separation effect. Larger source-detector separations (from 40 mm to 50 mm) extended the penetration of the fluence distribution to the grey matter in neonates but did not increase the penetration depth in the adult head model. Age differences in DOT sensitivity may be attributed to anatomical variations across ages. Increased scalp-to-brain distance was related to reduced path length through the brain regions in children (Whiteman et al., 2017). Moreover, greater scalp and skull thickness was associated with reduced sensitivity to the gray matter across source-detector separations from 20 mm to 50 mm in adults (Strangman et al., 2014). These studies conclude that age-related changes head/brain anatomy and composition affect the DOT sensitivity function. However, these studies are based on a limited range of ages (e.g., neonate; 5 to 11 years) and do not cover the age span across infancy when dramatic development of the head and brain occur.

The Applications of DOT Sensitivity

The DOT sensitivity profile provides a measure of the scalp-location-to-cortex correspondence. Fu and Richards (under review) estimated the distance between the scalp and the maximum fluence for the S-D Channel DOT fluence. They found that scalp-to-cortex distance increased from infancy to childhood and from childhood to adulthoods. This confirmed that longer source-detector separations are required for adults to achieve comparable depth sensitivity. The S-D Channel fluence distribution can also be used to localize the regions of interest (ROIs) that would be sampled with NIRS. Zimeo Morais, Balardin, and Sato (2018) used the S-D Channel DOT fluence to compute the specificity of each channel (10-10 electrode

pairings) in measuring the corresponding ROIs and non-brain tissues. Fu and Richards (under review) also used the S-D Channel DOT measure to map 101-10 channel locations with underlying ROIs from macro- and micro-structural atlases. Such channel-to-ROI look-up tables facilitate the optimization of channel array design to maximize DOT sensitivity to user-specified ROIs (Brigadoi, Salvagnin, Fischetti, & Cooper, 2018; Zimeo Morais et al., 2018) and help to localize the possible ROIs that generated the fNIRS signals (Bulgarelli et al., 2019; Bulgarelli et al., 2020; Perdue et al., 2019).

The Present Study

The current study examined age-related variations in DOT sensitivity profiles. Our primary contribution was to use existing methods for DOT sensitivity across the period of infancy (2 weeks through 24 months) with narrow age bands, and compare these to older children (4, 12 years) and adults (20-24 years). We used the MCX photon migration simulation program to model photon propagation through the segmented tissues in the individual head MRIs (Fang & Boas, 2009a; see Supplemental Information for further information). We estimated fluence distributions from the simulations. We depicted changes in DOT sensitivity profiles as a function of source-detector separation distances. The present study has important implications in the design of developmentally appropriate channel placements for NIRS recordings and make anatomical interpretations of stand-alone NIR data across a wide range of age groups.

Method

Participants

The participants were 1058 typically developing participants ranging from 2 weeks to 24 years of age. The MRIs were obtained from open-access databases and a local scanning facility. Details of the sample are described in (Fu & Richards, under review). Table 1 presents the number of MRIs for the open access databases, separately for age and gender. The sample ages were narrowest in the infancy period (2 weeks, 1-, 1.5-, 3-, or 6-month intervals from 2 weeks through 2 years) and included exemplar ages in children and adolescent ages (4, 12 years) and adult (20-24 years). All studies had institutional review board approval and informed consent for participants.

Table 1. Demographical information of study participants by age group, sex, and data source. *Note.* ABIDE=Autism Brain Imaging Data Exchange; BCP=Baby Connectome Project; EBDS=Early Brain Development Study; IBIS=Infant Brain Imaging Study; MCBI=McCausland Center for Brain Imaging; PING=Pediatric Imaging, Neurocognition, and Genetics Data Repository

Participant Information			**Data Source**					
Age Group	**Total *N***	**Female *N***	**ABIDE *N***	**BCP *N***	**EBDS *N***	**IBIS *N***	**MCBI and Collaboration Sites *N***	**PING *N***
2 Weeks	41	24	0	3	38	0	0	0
1 Month	96	40	0	17	79	0	0	0
2 Months	68	40	0	8	60	0	0	0
3 Months	38	21	0	24	0	0	14	0
4.5 Months	54	29	0	41	0	0	13	0
6 Months	74	35	0	0	0	60	14	0
7.5 Months	61	17	0	0	0	49	12	0
9 Months	60	35	0	48	0	3	9	0
10.5 Months	42	21	0	40	0	0	2	0
12 Months	109	36	0	0	0	89	20	0
15 Months	78	41	0	63	0	8	7	0
18 Months	76	31	0	36	0	8	32	0
2 Years	74	22	0	0	0	65	1	0
4 Years	24	9	0	0	0	0	10	14
12 Years	37	14	9	0	0	0	28	0
20-24 Years	134	77	0	0	0	0	134	0

MRI Sequences

The present study utilized T1-weighted (T1W) and T2-weighted (T2W) scans from each collection site. Details of the MRI acquisition protocols have been described in literatures on the Neurodevelopmental MRI Database (Fillmore, Phillips-Meek, & Richards, 2015; Fillmore, Richards, Phillips-Meek, Cryer, & Stevens, 2015; Richards, in prep; Richards, Sanchez, Phillips-Meek, & Xie, 2015; Sanchez, Richards, & Almli, 2012a, 2012b). All MRIs were converted to NIFTI compressed format with 32-bit floating point resolution. Bias-field inhomogeneity correction (N4 algorithm) was performed on the extracted T1-weighted images (Avants et al., 2011; Tustison et al., 2010).

MRI Preprocessing and Segmentation

First, the brains were extracted from the whole-head MRI volume in a procedure adapted from the FSL VBM pipeline (Douaud et al., 2007). The T1W volume for each participant was registered to an age-appropriate average MRI template. The MRI templates came from the Neurodevelopmental MRI database (Richards, Sanchez, et al., 2015; Sanchez et al., 2012a, 2012b). The brain from the average template was transformed into the participant MRI space and used a mask on the head volume. The extracted masked data was then used with the FSL brain extraction tool program (Jenkinson, Pechaud, & Smith, 2005; Smith et al., 2004). Each brain was visually inspected and manually modified if necessary. Second, each head MRI volume was segmented into 9 or 10 media types: gray matter (GM), white matter (WM), cerebrospinal fluid (CSF), non-myelinated axons (NMA), other brain matter, skin, skull, air, eyes, and other inside skull material. Details of the segmentation methods are presented in the Supplemental Information. The segmented regions were assembled into a single MRI volume we will refer to as the “segmented head MRI volume”. Figure 1A shows a 3D rending of the T1W volume from

a 3-month-old infant with a cutout revealing the segmented MRI volume. The realistic head model represents the geometry of the head and allow us to differentiate optical properties of different tissue types.

Mesh Generation

A “finite element method” (FEM) tetrahedral mesh was constructed from the segmented head MRI volume. Figure 1B and 1C displayed meshes that were produced using the iso2mesh toolbox with CGAL 3.6 mesh program ("v2m" function, Fang & Boas, 2009b). Tetrahedral meshes accurately represent boundaries of complex three-dimensional volumetric tissues and increase the accuracy in modeling photon propagation in the complex mediums such as the head and brain (Yan, Tran, & Fang, 2019). The FEM volumetric meshes have nodes that represent the voxel locations for the tetrahedra, a 4-element matrix representing the corners of each tetrahedron, and a vector representing the media type from the segmented head MRI volume. A mesh was generated for each segmented head MRI volume. Figure 1B depicts an example of the dense meshes. The number of nodes, elements, and tetra volume were calculated for the infants (2 weeks through 2 years), children (4 and 12 years), and adults (Supplemental Figure 1). We will refer to this as the “segmented FEM mesh”. We used the mesh to locate points on the scalp that were closest to the electrode positions.

A. B. C.

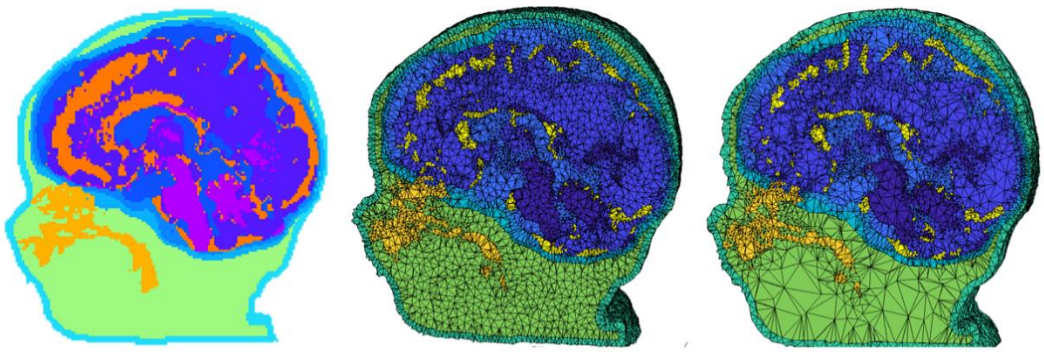

Fig 1. Segmented head MRI volumes. The examples were taken from the same 3-month-old infant MRI. A. The segmented head model. Aqua is the skull, purple is the gray matter, magenta is the white matter, dark orange is the cerebrospinal fluid, light blue is the dura, light orange is the nasal and mouth air cavities, and green is the non-bone structure (muscle, sinew, fat). B. The segmented head model with dense finite element model (FEM) mesh. C. The segmented head model with sparse FEM mesh.

Scalp Locations

Virtual Electrodes Placement

The locations for the 10-10 and 10-5 electrode systems were constructed on each head MRI volume. First, we manually marked cranial fiducial points using MRIcron (Rorden, 2012; Rorden & Brett, 2000): nasion (Nz), vertex (Vz), inion (Iz), left preauricular point (LPA), right preauricular point (RPA), left mastoid (LMa), and right mastoid (RMa) (Richards, Boswell, Stevens, & Vendemia, 2015). The coordinates of the fiducials were transferred on to the scalp mesh. Next, we calculated 81 virtual electrode positions based on the "unambiguously illustrated 10-10 system (Jurcak, Tsuzuki, & Dan, 2007). Details for constructing the 10-10 locations are described in Richards, Boswell, et al. (2015) and the Supplemental Information. We simulated a total of 358 electrodes on 10-5 locations by calculating center points between 10-10 positions. The electrode positions also were computed for the average MRI templates. Figure 2 illustrates the placements of 10-10 and 10-5 electrodes positions.

Source-Detector Channels, All Electrode Pairs

Source-detector channels were defined in three ways for the analyses. *Source-Detector Channels*: Source-detector channel locations were defined for some analyses using electrode combinations centered on each 10-10 electrode. The 10-10 electrode locations were centered between surrounding adjacent pairs of 10-10 or 10-5 electrode locations. There were 251 source-detector pairs formed with adjacent 10-10 electrodes, $Mean_{\text{Separation}}$ = 57.95 mm; *SD* = 14.22, and 251 pairs formed with adjacent 10-5 electrodes, $Mean_{\text{Separation}}$ = 28.92 mm; *SD* = 7.06. The channel locations were used to estimate "S-D Channel DOT fluence" described below. *All Electrode Pairs*: Some channel locations were defined from the combination of all 10-5 electrode positions for the source-detector distance analyses. The path from each electrode to all

other electrodes was traced on the scalp and the distance of the path recorded (63,903 paths). The channel location was defined at the half-way point in this path, and the electrode pairs, scalp path distance, and channel location were recorded. The channel locations identified using all electrode pairs were used to quantify specific source-detector separation distances for the depth sensitivity profile analysis described below.

A.

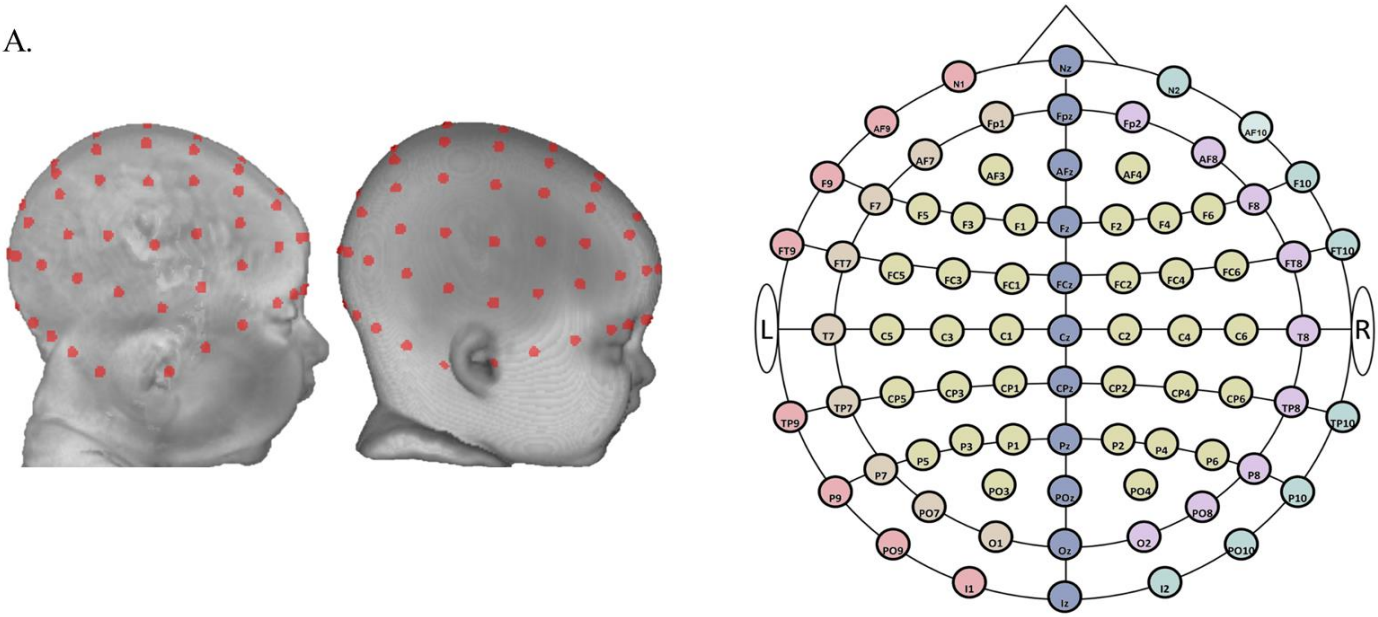

B.

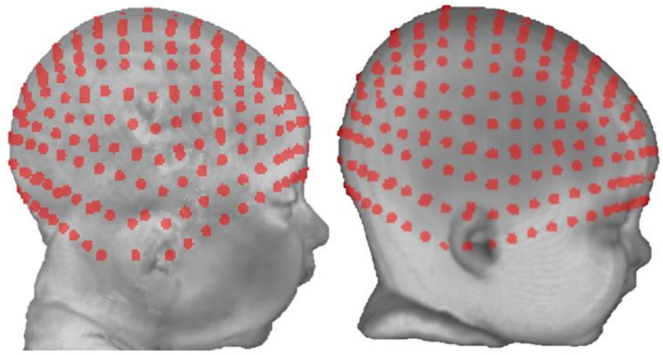

Fig 2. Virtual electrode placement. A. Ten-ten virtual electrode placement. From left to right: a three-month individual head model, an average template for three-month-olds, and a two-dimensional layout of the 10-10 system). Ten-ten electrodes were divided into six groups for visualization purposes. The six groups were color-coded on the two-dimensional schematic of the 10-10 system. Group 1: electrodes on the central curve (Nz-Cz-Iz). Group 2: electrodes on the left curve between Nz and Iz (N1-LPA/T9-I1). Group 3: electrodes on the right curve between Nz and Iz (N2-RPA/T10-I2). Group 4: electrodes on the left curve between Fpz and Oz (Fp1-T7-O1). Group 5: electrodes on the right curve between Fpz and Oz (Fp2-T8-O2). Group 6: the remaining electrodes enclosed by the central curve, the left and right curves between Fpz and Oz. B. Ten-five virtual electrode placement. From left to right: the same three-month individual head model and the three-month average template.

Photon Migration Simulations

The DOT fluence values were estimated with photon migration simulations. We modeled photon migration through brain tissues using the Monte Carlo eXtreme package (MCX; Fang & Boas, 2009a; Fang & Yan, 2019). The package implements an GPU-accelerated, voxel-based Monte Carlo simulation algorithm. We launched 10^8 photons for the time window of 0 to 5 nanoseconds. The fluence resolution was 50 time-gates (Zimeo Morais et al., 2018). The wavelength was set at 690 nanometers. Photons were sent from the 358 10-5 electrode positions. The optical properties of the 10 tissue types were set in accordance with previous studies by Perdue et al. (2019) and Fang (2010) which came primarily from Strangman, Franceschini, and Boas (2003) and Yaroslavsky et al. (2002). Table 2 contains the values that were used. It should be noted that there has been no consensus on the optical properties in the literature (Zimeo Morais et al., 2018). The values differ considerably across studies (Boas et al., 2002; Brigadoi & Cooper, 2015; Custo et al., 2010; Strangman et al., 2003; Strangman et al., 2013; Whiteman et al., 2017; Zimeo Morais et al., 2018). It is likely that different values are needed for adults versus developmental samples (Fukui et al., 2003). We have compiled optical properties used in published studies in Supplemental Information Table 1.

The Monte Carlo simulations estimate fluence distribution (Boas et al., 2002; Strangman et al., 2013). The photons were injected at the electrode position. The “flux” strength of the photons, or “fluence” of the sum photon flux, decreased monotonically due to absorption and scattering as photons traveled through brain tissues. The simulations accounted for absorption, scattering and reflection based on the specified optical properties (Boas et al., 2002; Fang & Boas, 2009a). Each simulation continued until the photon exited the media, was absorbed by the media, or after 5 nanoseconds. The output of the simulations included the photon fluence at each

nanosecond for each voxel from the injected photons. The number ranged from zero to the total number of injected photons. We summed this value across the 5 nanoseconds of the simulation. This value represents the fluence of the simulation. We took the log (fluence) as our number representing the DOT sensitivity for each voxel. Figure 3 shows the DOT fluence plotted on an individual subject MRI for a single electrode location. The gradual monotonic decrease in fluence as a function of partial path length may be seen in this figure.

Table 2. Optical properties used in Monte Carlo photon migration simulations. μ_a is the optical absorption coefficient; μ_s is the scattering coefficient, g is the anisotropy coefficient, and N is the index of refraction.

Tissue Type	μ_a **(mm^{-1})**	μ_s **(mm^{-1})**	g	N
White matter	0.07	40.1	0.85	1.37
Gray matter	0.02	8.4	0.90	1.37
CSF	0.0004	1	0.99	1.37
Dura	0.0101	80	0.99	1.37
Skull	0.0101	100	0.99	1.37
Skin	0.0101	80	0.99	1.37
Muscle	0.0101	80	0.99	1.37
Eyes	0.0004	1	0.99	1.37
Nasal Cavity	0.0101	80	0.99	1.37
Non-myelinated Axons	0.07	40.1	0.85	1.37

DOT Sensitivity Analyses

The output from the Monte Carlo simulation contained the fluence across the entire MRI volume separately for each electrode. We simulated the path for several analyses from a source-electrode (optode) to a detector-electrode (optode). This was done by multiplying the source-electrode (optode) fluence distribution by the detector-electrode (optode) fluence distribution. We will refer to this as “S-D Channel DOT fluence”. This represents the DOT fluence sensitivity for a photon channel from the source to the detector ("PMDF" in Brigadoi & Cooper, 2015). An ad-hoc method has been used in some studies to divide the product by the estimated value of the photons from the source in the vicinity of the detector (Perdue, Fang, & Diamond, 2012). This step was not taken in the current study. Figure 3 shows the S-D Channel DOT fluence plotted on an MRI for a single source-detector pair. This figure shows a similar monotonic decrease in fluence strength as a function of partial path length.

Depth Sensitivity Profile by Source-Detector Separation Distances

We examined how the depth sensitivity of S-D Channel DOT changed as a function of source-detector separation distance. The target source-detector separation distances for testing were from 10 mm to 60 mm by 5 mm increments. They were selected from “all electrode pairs”. Supplemental Information Table 2 lists the minimum and maximum separation distances for each target separation distance for all age group. Supplemental Information Figure 2 displays the mean number the source-detector channels with the target separation distances by age group. The S-D DOT fluence sensitivity function was defined as the fluence value at the voxel as a function of the distance (depth) from the channel location to the voxel (PPL; Mansouri et al., 2010; Strangman et al., 2014; Wang et al., 2019). We additionally assessed the variance of the sensitivity profile by examining the standard error of the mean fluence value as a function of

PPL. The shape of the S-D DOT fluence distribution was quantified by the half-width half-maximum (HWHM; Kumar Reddy & Sagar, 2015). The HWHM identified the PPL location at which the fluence first dropped below half of the maximum value. We referred to this as the HWHM location.

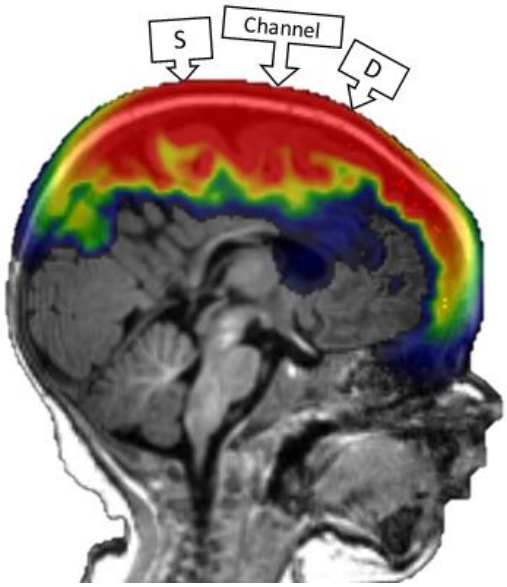

Fig 3. Source-Detector (S-D) Channel DOT fluence distribution. Monte Carlo photon migration simulations were used to estimate fluence distributions. The red area represents greater fluence.

Results

Depth Sensitivity Profiles by Source-Detector Separation Distances

We examined the S-D Channel DOT fluence as a function of penetration depths (PPL) sampled in the fluence distribution. This was done by selecting 10-5 location pairs with separation distances from 10 mm to 60 mm by 5 mm increments and calculating the S-D Channel DOT fluence for each pair and averaging over pairs of the same distance. Figure 4 displays examples of the depth sensitivity profiles plotted by channels (separate lines) and separation distances (panels) for one individual from four different ages at 20 mm and 50 mm separations (more examples are displayed in Supplemental Information Figures 3A and 3B). The sensitivity profiles across the four individuals showed greater peaks and steeper slopes for channels at 20 mm than 50 mm separation. The between-channel variance showed a systematic decline from the infants to the adults. The variance increased from 20 mm to 50 mm separations for the infant groups whereas it remained stable for the adult group.

The sensitivity profiles changed with separation distances across age groups. Figure 5A shows the S-D Channel DOT fluence as a function of partial path length (PPL) separately for the target source-detector distances, averaged across channel locations, and separately for four age bins. We grouped the samples to four age bins for averages for some analyses based on preliminary data visualization: 2 weeks through 4.5 months; 6 months through 12 months; 15 months through 2 years; 4, 12, and 20-24 years. The sensitivity profile changed systematically with the source-detector distance. The peak of the sensitivity function was largest at the smallest separation distance and decreased as source-detector distance increased. However, the fluence value dissipated more quickly at the shorter source-detector distances than the longer distances, with the distributions becoming flatter across increasing source-detector distance. Compared to

the sensitivity profile at shorter separation distances, the same fluence value was carried to greater penetration depth at larger separation.

The patterns of age-related differences in the sensitivity profiles were relatively consistent across separation distances. Figures 5B, 5C, and 5D show the S-D Channel DOT fluence sensitivity functions for the 20 mm, 30 mm, and 50 mm source-detector separations, respectively, and separately for the testing ages. There were consistent age changes in the shape of the sensitivity function over the source-detector separations. These are most easily seen in the profile for the 50 mm separation (Figure 5D). The 2-week through 4.5 month old age groups (Figure 5A solid line, aqua color) had a relatively high peak and rapid decline, the 6-month-to-12 month ages (Figure 5A solid line blue color) and the 15-month to 2-year-old ages (Figure 5A dashed line red color) had a smaller peak value and less rapid decline, i.e., flatter shape. These age differences were similar across all source-detector distances but became greater with increasing source-detector distance.

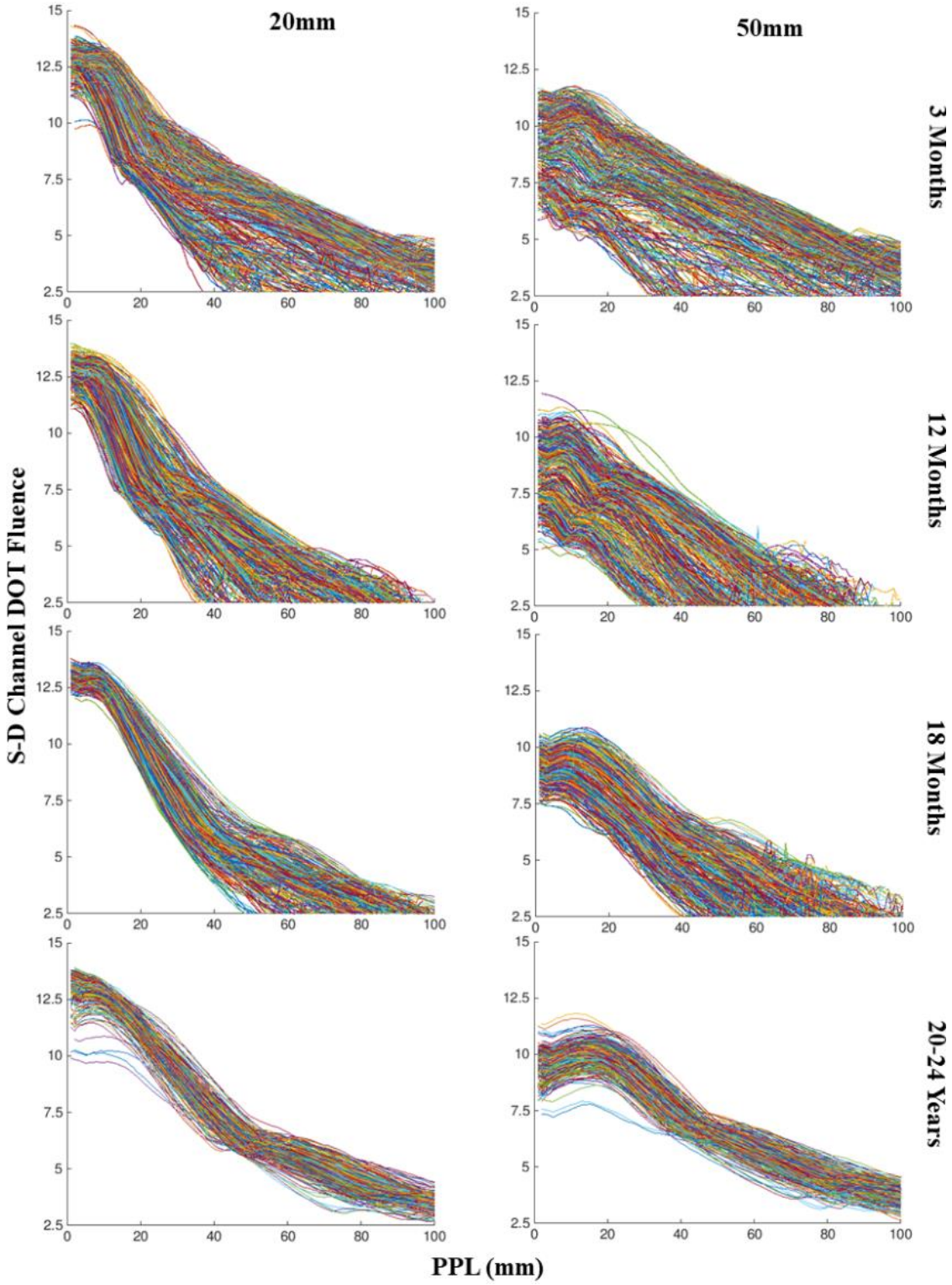

Fig 4. Source-Detector (S-D) Channel DOT fluence sensitivity profile by channels. Four example individuals were selected, one from each age category. The S-D Channel DOT fluence value was plotted as a function of the partial path length (PPL) separately for channels at the source-detector separations for 20 mm and 50 mm for each individual.

A.

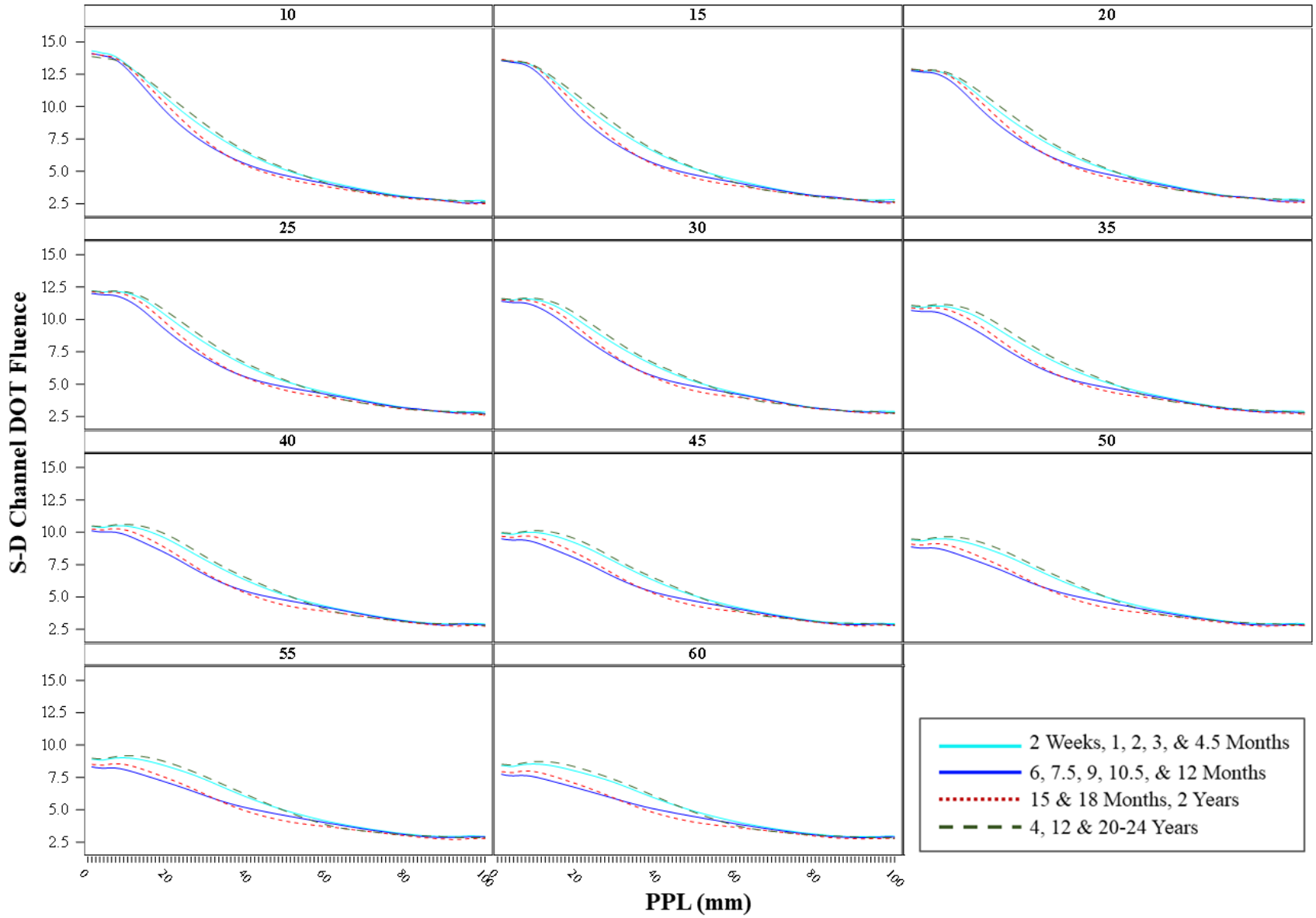
10
15
20
25
30
35
40
45
50
55
60
S-D Channel DOT Fluence
15.0
12.5
10.0
7.5
5.0
2.5
0
20
40
60
80
100
PPL (mm)
2 Weeks, 1, 2, 3, & 4.5 Months
6, 7.5, 9, 10.5, & 12 Months
15 & 18 Months, 2 Years
4, 12 & 20-24 Years

B.

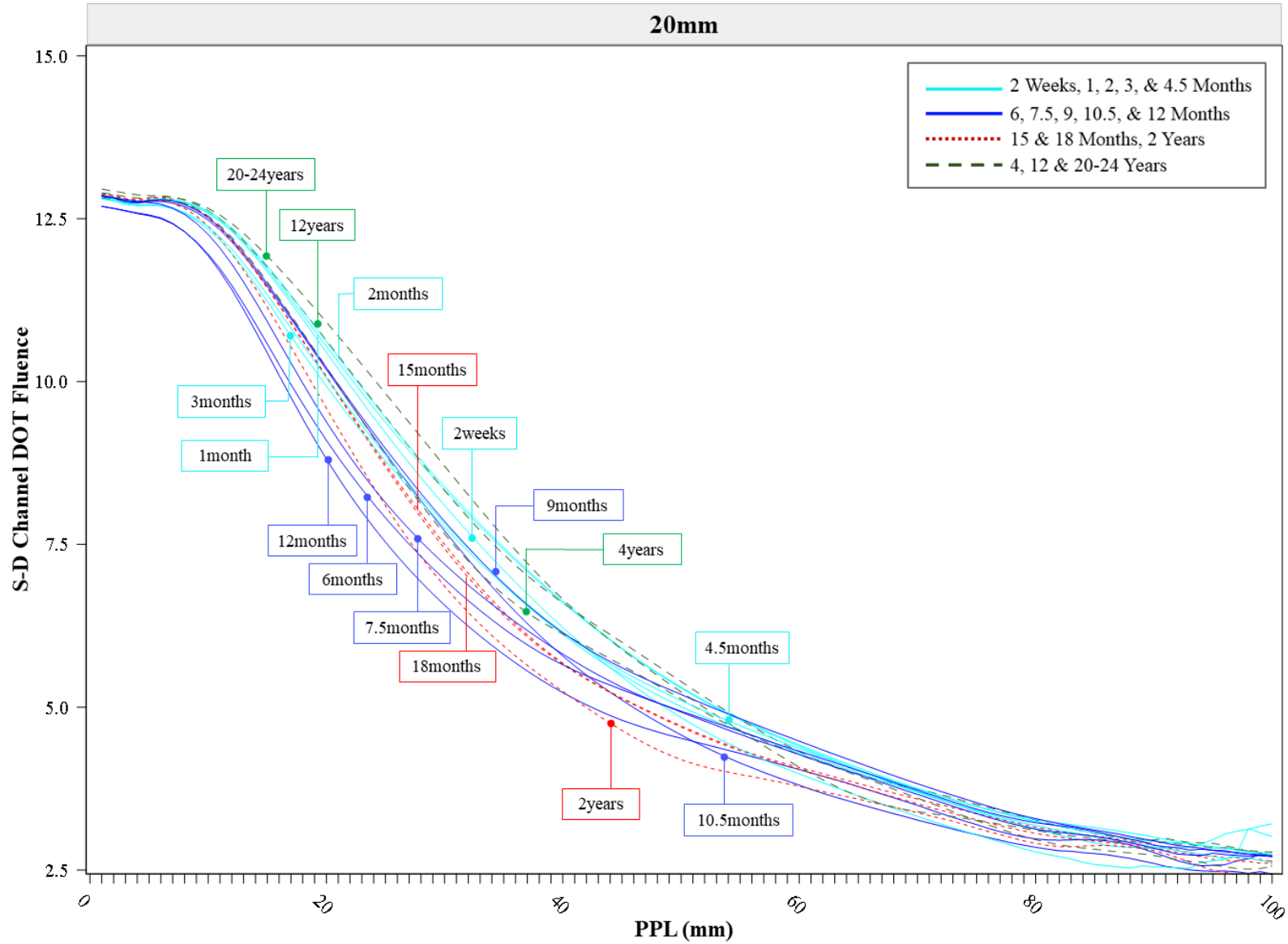
20mm
2 Weeks, 1, 2, 3, & 4.5 Months
6, 7.5, 9, 10.5, & 12 Months
15 & 18 Months, 2 Years
4, 12 & 20-24 Years
20-24years
12years
2months
15months
3months
2weeks
1month
9months
12months
4years
6months
7.5months
4.5months
18months
2years
10.5months
S-D Channel DOT Fluence
15.0
12.5
10.0
7.5
5.0
2.5
0
20
40
60
80
100
PPL (mm)

C.

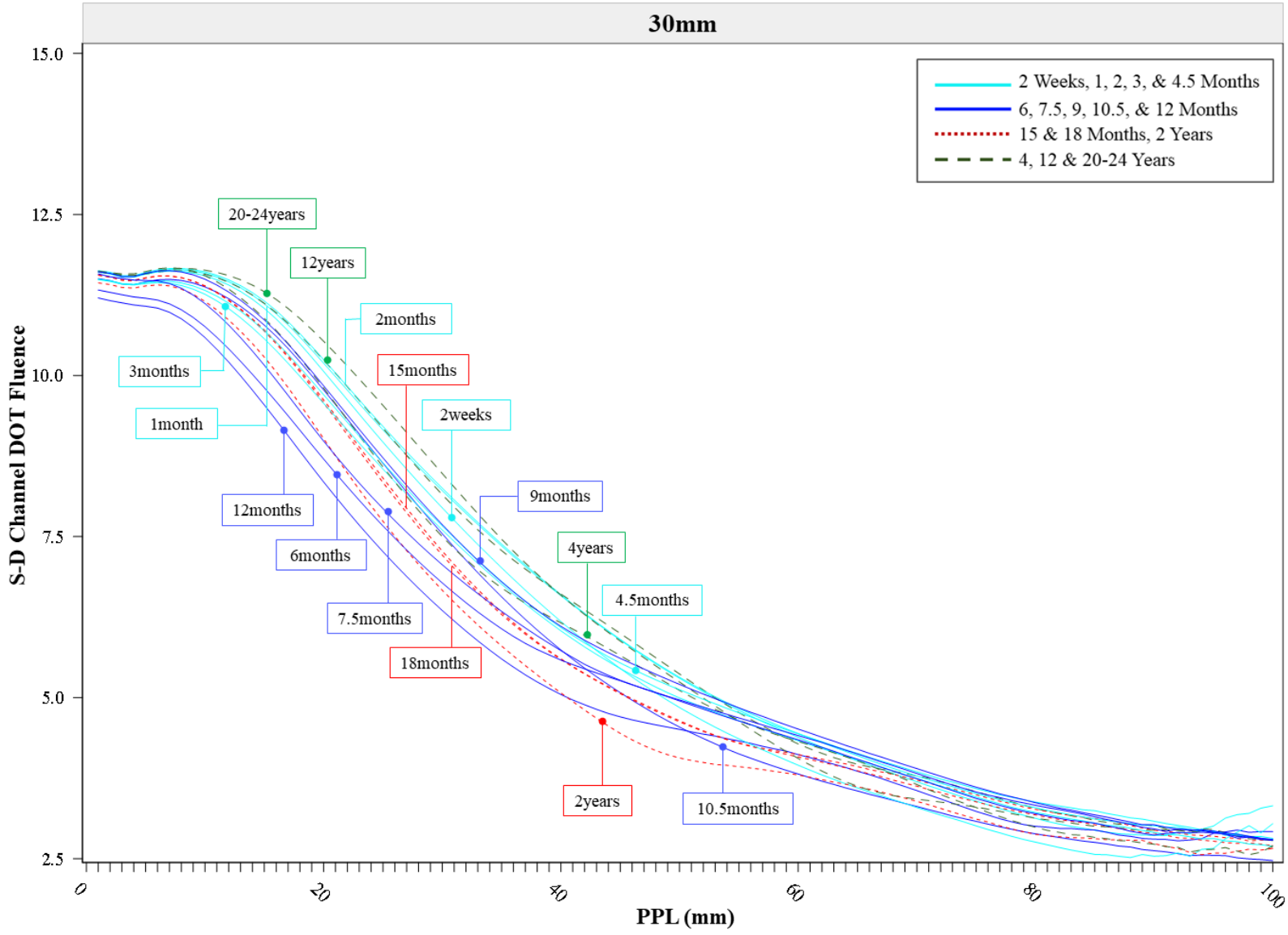
30mm
2 Weeks, 1, 2, 3, & 4.5 Months
6, 7.5, 9, 10.5, & 12 Months
15 & 18 Months, 2 Years
4, 12 & 20-24 Years
20-24years
12years
2months
3months
15months
1month
2weeks
9months
12months
4years
6months
4.5months
7.5months
18months
2years
10.5months
S-D Channel DOT Fluence
15.0
12.5
10.0
7.5
5.0
2.5
0
20
40
60
80
100
PPL (mm)

D.

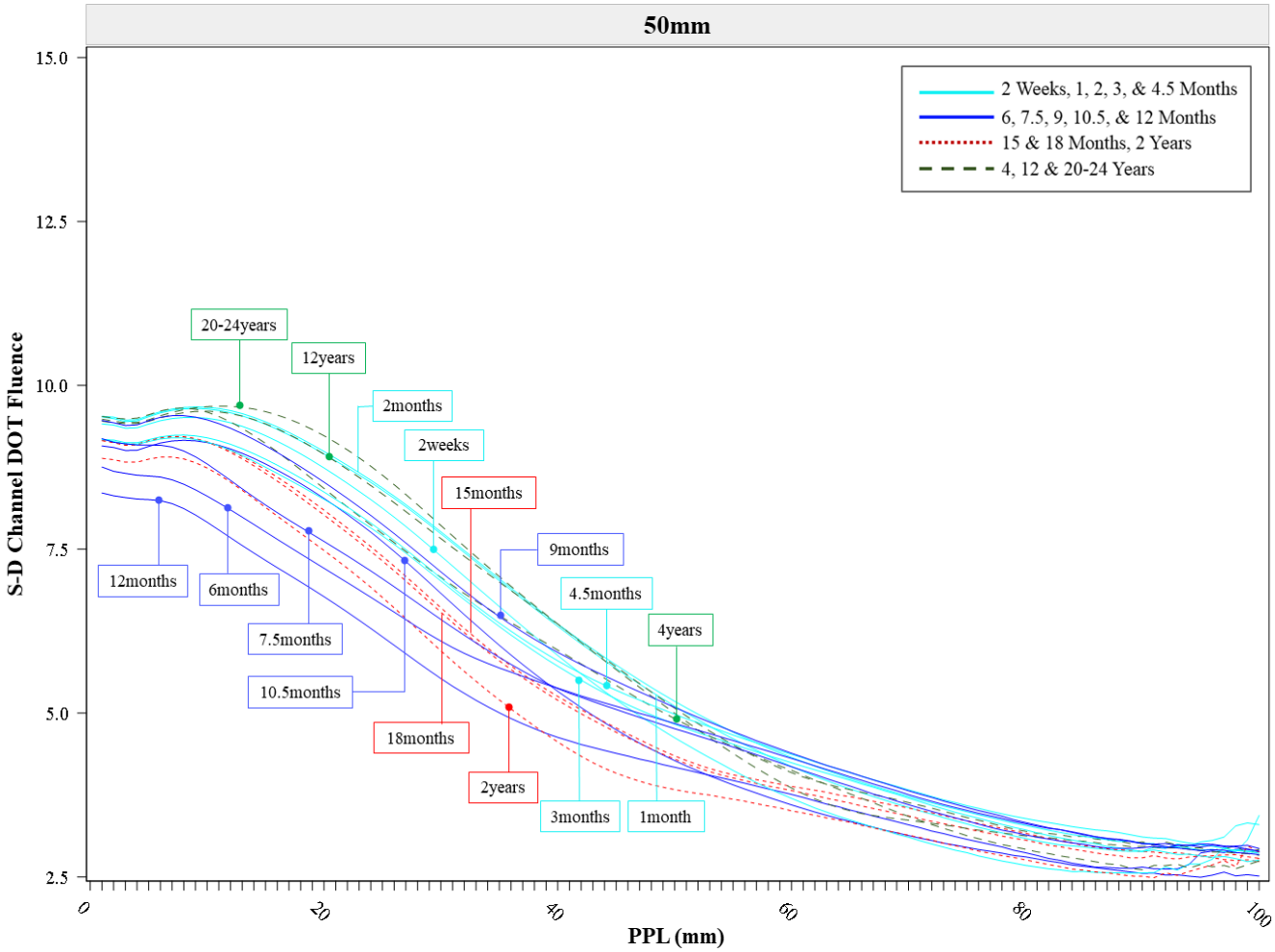

Fig 5. Source-Detector (S-D) Channel DOT fluence sensitivity profile by age groups. A. S-D Channel DOT fluence sensitivity function at each target source-detector separation distances. For visualization, we created four age categories: 2 weeks to 4.5 months, 6 months to 12 months, 15 months to 2 years, and 4 years to 20-24 years. Mean values by each age category are displayed. B. S-D Channel DOT fluence sensitivity function by individual age categories at 20 mm source-detector separation. C. S-D Channel DOT fluence sensitivity function by individual age categories at 30 mm separation. D. S-D Channel DOT fluence sensitivity function by individual age categories at 50 mm separation.

The Variance of S-D Channel DOT Fluence Sensitivity Profiles

We also examined the between-channel variance of the S-D Channel DOT fluence as a function of penetration depths. Figure 4 showed the average between-channel variance of the sensitivity profiles across separation distances, which apparently differed across ages and showed a larger change with source-detector separation for infants than adults. We further examined the variance by computing the average standard error of the mean S-D Channel DOT fluence value. Figure 6A displays the average of the standard error as a function of PPL for each separation distance. The average variance as a function of penetration depth increased at separation distances greater than 35 mm for the younger infants (2 weeks to 12 months). The average variance became larger with increased penetration depth for the infants between 15 months to 2 years of age at separation distances greater than 20 mm. The average variance across penetration depth significantly increased at 55 mm and 60 mm separations for the 15-month-to-2-year group. The average variance across penetration depth remained relatively stable for the child and adult group. Figure 6B shows the standard error of the mean S-D Channel DOT fluence value as a function of penetration depth separately by the testing age groups at 20 mm separation. The variance across penetration depth was the greatest for infants aged between 3 months to 2 years relative to the children and adults. The youngest infants (2 weeks, 1 month, 2 months) showed relatively small variability across separation depts. We present similar figures for 30 mm and 50 mm separations in Supplemental Information Figures 4A and 4B. These figures show that the variance as a function of penetration depth was greater at larger separations for all age groups. The age-related differences in variance were enhanced at 50 mm separations. The increase in variance at larger separation was more discernible for infants between 3 months to 2 years. The patterns of age-group differences in variance of the sensitivity profile across

separation distances were consistent with the individual-subject plots displayed in Figure 4 and Supplemental Information Figure 3.

A.

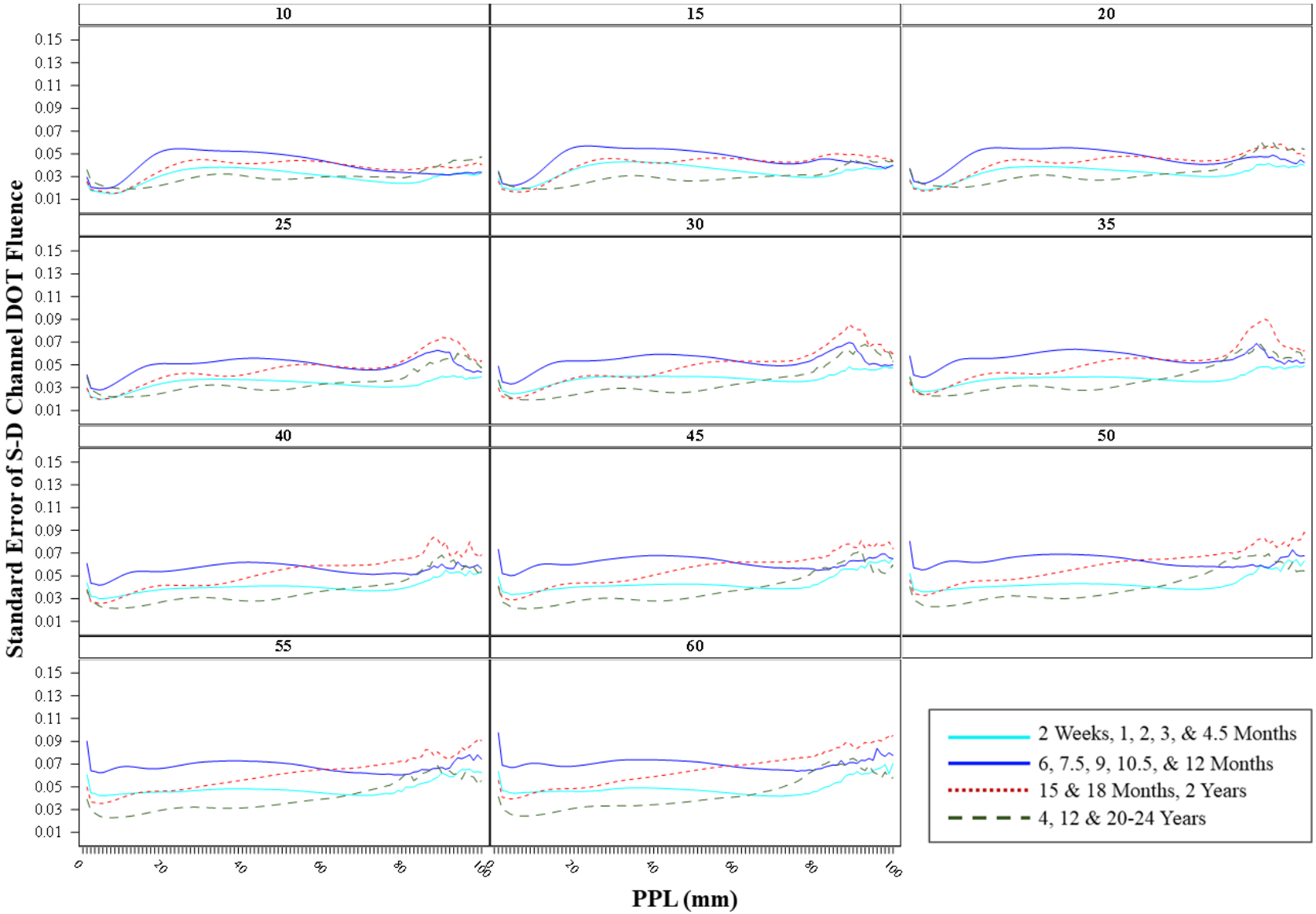
10
15
20
25
30
35
40
45
50
55
60
Standard Error of S-D Channel DOT Fluence
0.15
0.13
0.11
0.09
0.07
0.05
0.03
0.01
0
20
40
60
80
100
PPL (mm)
2 Weeks, 1, 2, 3, & 4.5 Months
6, 7.5, 9, 10.5, & 12 Months
15 & 18 Months, 2 Years
4, 12 & 20-24 Years

B.

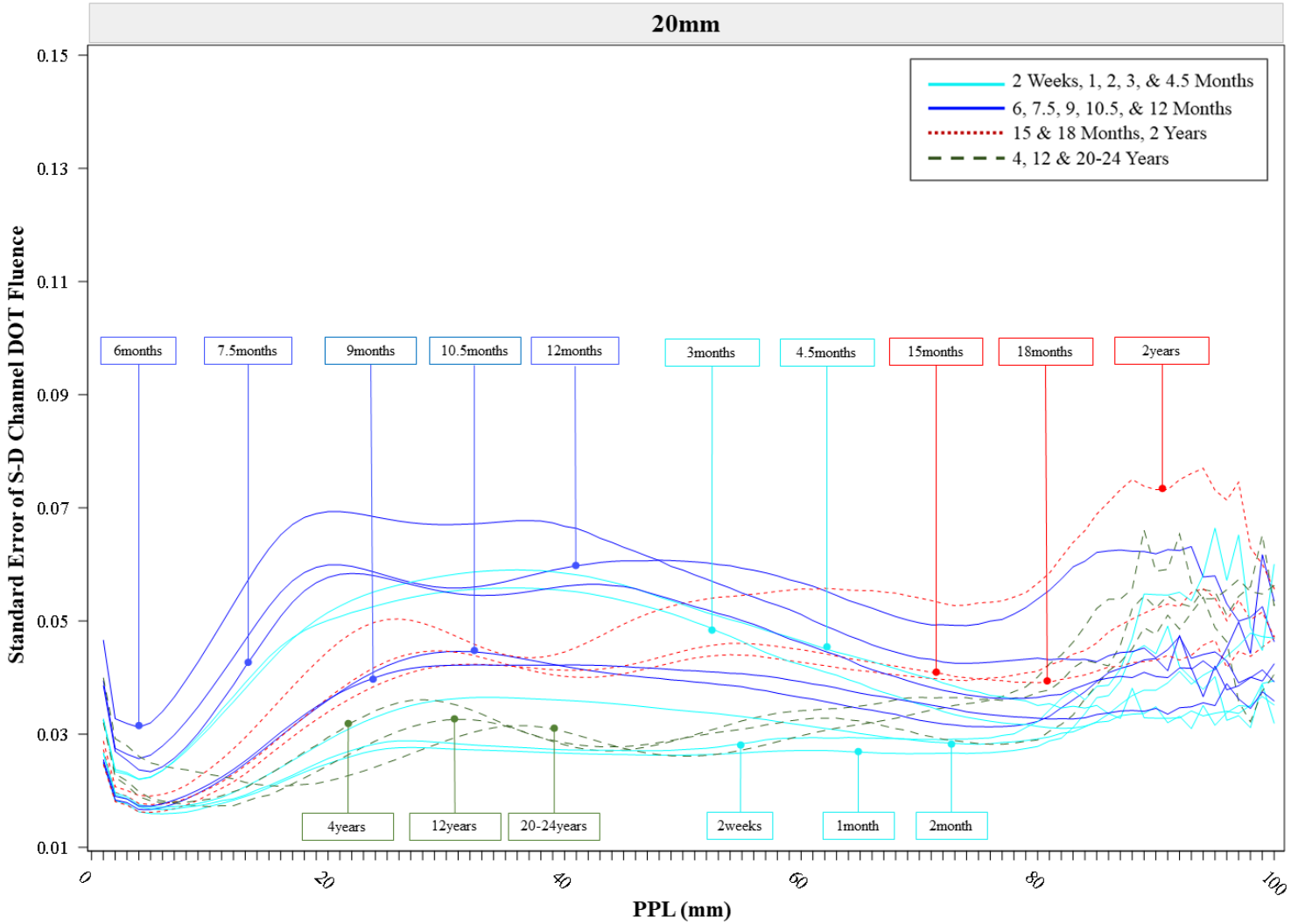

Fig 6. Variability of Source-Detector (S-D) Channel DOT fluence sensitivity profile. This is the standard error of the S-D Channel DOT fluence value as a function of the partial path length (PPL). A. Standard error of the S-D Channel DOT fluence sensitivity function averaged by the age categories. B. Standard error of the S-D Channel DOT fluence sensitivity function by individual age groups at 20 mm source-detector separation.

The Shape of S-D Channel DOT Fluence Sensitivity Profiles

The last analysis examined the half-width half-maximum (HWHM) location for each S-D Channel DOT fluence distribution. Figure 7 shows the HWHM location as a function of the source-detector distance separately for the testing ages, separately for all ages (Figure 7A) and for four separate age groupings (Figure 7B). The HWHM increased as a function of the source-detector distance. This increase quantifies the apparent change in steepness in the S-D DOT Channel fluence sensitivity functions over source-detector distances (Figure 5A). The change in HWHM across source-detector distance implies that there was a gain in sensitivity to deeper cortex over the source-detector distance, though the fluence strength systematically decreased with increasing source-detector distance (e.g., Figure 5A). The patterns of the HWHM location over age parallel the age differences found in the sensitivity profile (e.g., Figure 5A). The mean HWHM locations across all separation distances were greater in the youngest infants (2-week through 4.5 month old age groups, Figure 7A and 7B solid line, aqua color), at smaller levels in the 6-month-to-12 month ages (Figure 7A and 7B solid line blue color) and the 15-month to 2-year-old ages (Figure 7A and 7B dashed line red color). These differences were consistent with the age differences found in the sensitivity profile (e.g., Figure 5A). The larger HWHM location values for the youngest age group implies the DOT sensitivity to deeper cortical areas for the youngest ages.

A.

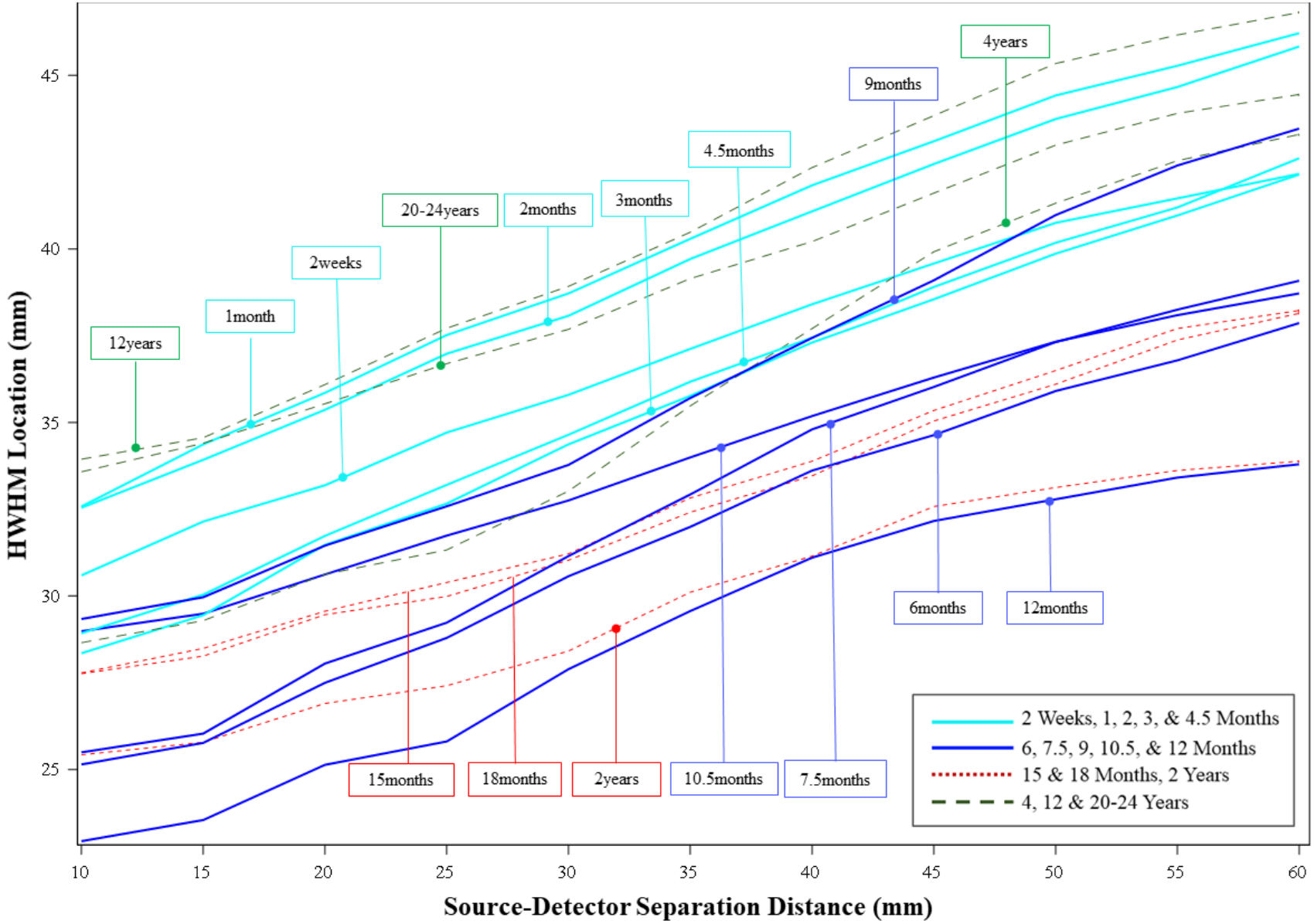
HWHM Location (mm)
Source-Detector Separation Distance (mm)
45
40
35
30
25
10
15
20
25
30
35
40
45
50
55
60
12years
1month
2weeks
20-24years
2months
3months
4.5months
9months
4years
15months
18months
2years
10.5months
7.5months
6months
12months
2 Weeks, 1, 2, 3, & 4.5 Months
6, 7.5, 9, 10.5, & 12 Months
15 & 18 Months, 2 Years
4, 12 & 20-24 Years

B.

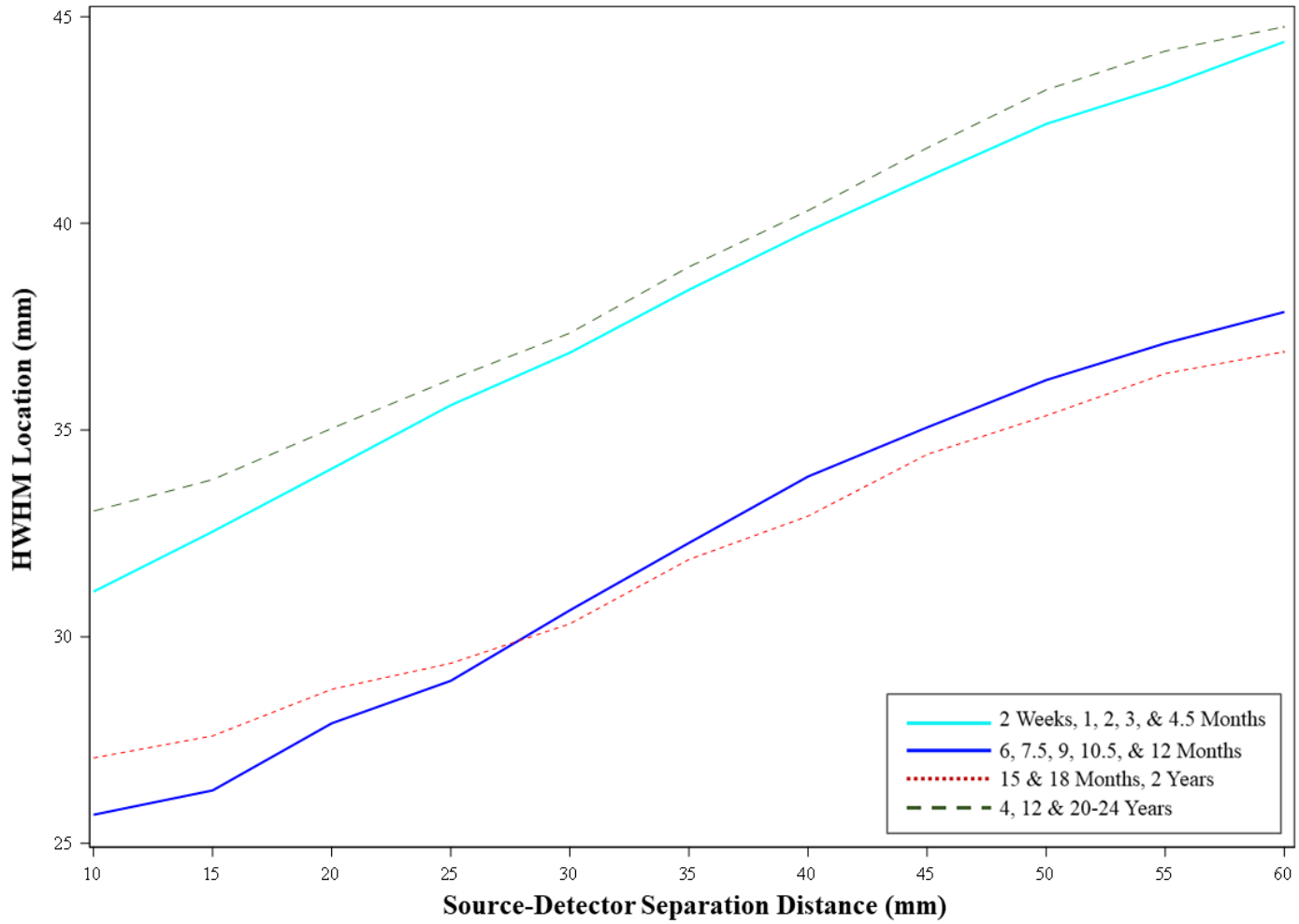

Fig 7. Half width half maximum (HWHM) locations of S-D Channel DOT fluence as a function of source-detector separation distances. The HWHM location was defined as the point in the fluence distribution at which the fluence first dropped below half of the maximum value. A. HWHM locations by source-detector separation distances for individual age groups. B. Mean HWHM locations by source-detector separation distances for the four age categories: 2 weeks to 4.5 months, 6 months to 12 months, 15 months to 2 years, and 4 years to 24 year.

Discussion

The present study examined age differences in DOT sensitivity profiles. We extended existing photon migration simulation methods to realistic head models from infants ranging from 2 weeks to 24 months, children (4, 12 years) and adults. The DOT sensitivity profiles had a common shape across source-detector separation and ages. There were expected differences in the depth sensitivity for source-detector separations, with larger separations being more sensitivity to greater cortical depths but showing decreasing signal strength and larger variance in the fluence measure. A noticeable age-group difference was that the fluence distribution penetrated greater depth with the same level of signal loss in the younger infant (2 weeks to 4.5months) than the rest of the infant age groups.

DOT Depth Sensitivity Profiles

The present study showed that the depth sensitivity profiles change systematically as a function of source-detector separation distance for all age groups. The study enhanced the DOT sensitivity estimation accuracy by using realistic FEM head models with refined segmentation of tissue types. The depth sensitivity profiles depict S-D Channel DOT fluence as a function of PPL sampled in the fluence distribution. The peak value of the S-D Channel DOT fluence was larger at shorter separation distances but with rapid decay as PPL increased. Alternatively, at larger separation distances there was a smaller peak value but with less rapid decline with increased PPL. The between-channel variance in the sensitivity profiles considerably increased with separation distances in infants. The increase was greater in older infants between 3 months to 2 years. The variance remained relatively stable for younger infants (2 weeks to 2 months), children, and adults.

The shape of the sensitivity profile was characterized by measuring the point in the fluence distribution where the fluence value first dissipated below half of the maximum value (i.e. “HWHM location”). The HWHM location increased with source-detector separation distance for all age groups. This indicates that there is a gain in sensitivity to deeper cortical structures with increased separations at the expense of decreased signal strength. We replicated the robust characteristics of the DOT sensitivity profiles found in existing studies that modeled photon migrations in head models from infants (Fukui et al., 2003) and adults (Mansouri et al., 2010; Strangman et al., 2013; Strangman et al., 2014; Wang et al., 2019). The trade-off between the gain in sensitivity to deeper cortical regions and loss in signal strength and spatial resolution needs to be considered in the design of source-detector separation distances.

The depth sensitivity profiles showed relatively consistent age-related differences across source-detector separation distances. Young infant groups (2 weeks to 4.5 months) displayed a sensitivity profile that was significantly different from the older infant groups (6 months to 2 years). The sensitivity profiles for the young infant groups at all separation distances were characterized by higher peaks and steeper decreases of S-D Channel DOT fluence values with increased PPL. Their sensitivity profiles displayed relatively stable variance across separation distances. The sensitivity profiles for the older infant groups were characterized by smaller peaks and more gradual declines with increased PPL. Their sensitivity profiles showed greater variance at larger separations. The slopes of increase in HWHM location across source-detector distance were similar across age groups. This suggests that the gain in depth sensitivity by increasing separation distances is comparable across age groups.

Applications of Age-specific DOT Sensitivity Profiles

DOT sensitivity profiles can be used with scalp-to-cortex distance calculations to determine the appropriate source-detector separations for the target age group (Whiteman et al., 2017). NIRS studies conventionally use 20mm to 30mm separations for infants (Gervain et al., 2011; Lloyd-Fox, Blasi, & Elwell, 2010) and 30mm to 35mm for children (e.g. Ding, Fu, & Lee, 2014; Perlman, Luna, Hein, & Huppert, 2014) and adults (Pinti et al., 2020). Young infants and adults displayed comparable DOT sensitivity profiles at 20mm-to-30mm separation. However, Fu and Richards (under review) showed that young infants had closer scalp-to-cortex distances than adults (3 months: 8mm; 20-24 years: 13mm). Hence, young infants may have greater DOT sensitivity to the cortex than adults (cf. Fukui et al., 2003). The main effect of age groups was more discernible at larger separations. Increasing separation distances to 35mm or greater may cause more concern in terms of reduction of signal strength and increased variance with relatively less gain in improving sensitivity to the cortex for older infants compared to adults.

Detailed descriptions of changes in DOT sensitivity profiles by separation distances across developmental and adult samples can better inform the design of channel/optode placement. A number of studies have used the S-D channel DOT fluence measure to estimate the mapping between channel locations and ROIs (Bulgarelli et al., 2019; Bulgarelli et al., 2020; Fu & Richards, under review; Perdue et al., 2019; Zimeo Morais et al., 2018). For example, Zimeo Morais et al. (2018) provided a toolbox that displays the channels that measure the user-specified ROI with a specificity value (1%-100%) for each channel. For the selected candidate channels, the users can also obtain their specificity to measure other (non-selected) brain regions. The channel(s) that show good discrimination to the user-selected ROI (i.e., high specificity to the ROI and low specificity to other brain and non-brain regions) are desirable. However, the

toolbox uses a pool of 130 10-10 channels that have a relatively fixed separation distance for the adult head model (median=3.60cm, lower quartile=3.13cm, upper quartile=3.98cm; Zimeo Morais et al., 2018). The toolbox and existing look-up tables do not consider that the separation distance for a given electrode pairing changes with age as head sizes get bigger. Additionally, the current findings indicate that the separation-related changes in sensitivity profile also vary by age groups. Increasing channel separation beyond 30mm for infants may reduce the channel-to-ROI discrimination. This is problematic especially when researchers use ROIs from micro-structure atlases and are interested in comparing results between age groups. Future tools for designing channel placements should allow users to optimize the constellation of electrode locations based on ROIs, age group, and separation distances.

The age-related differences in sensitivity profiles reinforce the importance of using age-appropriate head models for DOT image reconstruction. The sensitivity profile estimated from MC photon migration simulations can be recorded in a forward matrix. This is then used for solving the inverse problem in DOT image reconstruction that localizes the ROIs that showed hemoglobin concentration changes (Cooper et al., 2012; Culver et al., 2003). Contemporary toolboxes for DOT image source reconstruction (AtlasViewer: Aasted et al., 2015; TOAST++: Schweiger & Arridge, 2014) use adult head models as the default option. The present study provides data that show the importance of using age-appropriate templates as an anatomical prior to improve accuracy in channel location co-registration and forward model estimation. Wijeakumar, Kumar, Delgado Reyes, Tiwari, and Spencer (2019) and Delgado Reyes, Wijeakumar, Magnotta, Forbes, and Spencer (2020) show examples of this. They selected head models with atlas parcellations from the Neurodevelopmental MRI database (Richards, in prep; Richards, Sanchez, et al., 2015; Sanchez et al., 2012a, 2012b) that were closely matched in age

of the participants (4-month to 2-year-olds: Delgado Reyes et al., 2020; 4- to 48-month-olds: Wijeakumar et al., 2019). The head models were used for estimating the forward model and image reconstruction using the AtlasViewer (Aasted et al., 2015). The resultant voxel-wise hemodynamic concentration estimates were then entered in group-level analyses.

Limitation

The current study did not compute DOT sensitivity by tissue types separately. Existing evidence indicated that the change of relative sensitivity as a function of source-detector separation distance displayed different shapes for GM, WM, CSF, and extracerebral tissues (scalp and skull) in infants and adults (Fukui et al., 2003; Mansouri et al., 2010; Strangman et al., 2013; Strangman et al., 2014). Our data could be used to evaluate the fluence strength to the cortex based on the S-D Channel DOT scalp-to-cortex distance and the depth sensitivity profiles. We also could directly compare the relative sensitive to the brain versus extracerebral tissues at different separation distances for infants and adults (Brigadoi & Cooper, 2015; Strangman et al., 2013). Future analyses that compare sensitivity profiles by tissue types could more precisely inform age-related differences in the optimal separation distances for sampling GM signal changes.

Conclusions

The current study examined DOT sensitivity profiles in infants, children, and adults. The profiles change systematically as a function of source-detector separation distance for all age groups. There were also important age-related differences in the DOT fluence depth sensitivity profile. These are particularly discernible between younger (2 weeks to 4.5 months) and older infants at larger separation distances. Our findings of age-related differences in DOT depth sensitivity profiles are useful in the analysis of age-appropriate source-detector distances that

match sensitivity, signal strength, and depth for different ages. Our findings imply that accurate anatomical interpretations of NIRS/fNIRS data are dependent on developmentally sensitive estimations of DOT sensitivity that account for the head and cortical development. The present study demonstrated that age-appropriate realistic head models can be used with photon migration simulations to provide anatomical guidance for standalone DOT data.

Acknowledgement

This research was supported by grants from the National Institute of Child Health and Human Development (NICHD-R01-HD18942, NICHD-R37-HD18942, NIHCD-R03-HD091464) to J.E. Richards.

References

Aasted, C., Yücel, M., Cooper, R., Dubb, J., Tsuzuki, D., Becerra, L., . . . Boas, D. (2015). Anatomical guidance for functional near-infrared spectroscopy: AtlasViewer tutorial. *Neurophotonics, 2*(2), 020801. Retrieved from https://doi.org/10.1117/1.NPh.2.2.020801

https://www.ncbi.nlm.nih.gov/pmc/articles/PMC4478785/pdf/NPh-002-020801.pdf

Avants, B. B., Tustison, N. J., Song, G., Cook, P. A., Klein, A., & Gee, J. C. (2011). A reproducible evaluation of ANTs similarity metric performance in brain image registration. *Neuroimage, 54*(3), 2033-2044. doi:https://doi.org/10.1016/j.neuroimage.2010.09.025

Boas, D. A., Culver, J. P., Stott, J. J., & Dunn, A. K. (2002). Three dimensional Monte Carlo code for photon migration through complex heterogeneous media including the adult human head. *Opt Express, 10*, 159-170.

Brigadoi, S., Aljabar, P., Kuklisova-Murgasova, M., Arridge, S. R., & Cooper, R. J. (2014). A 4D neonatal head model for diffuse optical imaging of pre-term to term infants. *Neuroimage, 100*, 385-394. doi:10.1016/j.neuroimage.2014.06.028

Brigadoi, S., & Cooper, R. J. (2015). How short is short? Optimum source-detector distance for short-separation channels in functional near-infrared spectroscopy. *Neurophotonics, 2*(2), 025005. doi:10.1117/1.NPh.2.2.025005

Brigadoi, S., Salvagnin, D., Fischetti, M., & Cooper, R. (2018). Array Designer: automated optimized array design for functional near-infrared spectroscopy. *Neurophotonics, 5*(3), 035010. Retrieved from https://doi.org/10.1117/1.NPh.5.3.035010

https://www.ncbi.nlm.nih.gov/pmc/articles/PMC6135986/pdf/NPh-005-035010.pdf

Bulgarelli, C., Blasi, A., de Klerk, C. C. J. M., Richards, J. E., Hamilton, A., & Southgate, V. (2019). Fronto-temporoparietal connectivity and self-awareness in 18-month-olds: A resting state fNIRS study. *Developmental Cognitive Neuroscience, 38*, 100676. doi:https://doi.org/10.1016/j.dcn.2019.100676

Bulgarelli, C., de Klerk, C. C. J. M., Richards, J. E., Southgate, V., Hamilton, A., & Blasi, A. (2020). The developmental trajectory of fronto-temporoparietal connectivity as a proxy of the default mode network: a longitudinal fNIRS investigation. *Human Brain Mapping, 41*(10), 2717-2740. doi:10.1002/hbm.24974

Cooper, R. J., Caffini, M., Dubb, J., Fang, Q., Custo, A., Tsuzuki, D., . . . Boas, D. A. (2012). Validating atlas-guided DOT: a comparison of diffuse optical tomography informed by atlas and subject-specific anatomies. *Neuroimage, 62*(3), 1999-2006. doi:10.1016/j.neuroimage.2012.05.031

Culver, J. P., Siegel, A. M., Stott, J. J., & Boas, D. A. (2003). Volumetric diffuse optical tomography of brain activity. *Optics Letters, 28*(21), 2061-2063. doi:10.1364/ol.28.002061

Custo, A., Boas, D. A., Tsuzuki, D., Dan, I., Mesquita, R., Fischl, B., . . . Wells, W., 3rd. (2010). Anatomical atlas-guided diffuse optical tomography of brain activation. *Neuroimage, 49*(1), 561-567. doi:10.1016/j.neuroimage.2009.07.033

Delgado Reyes, L., Wijeakumar, S., Magnotta, V. A., Forbes, S. H., & Spencer, J. P. (2020). The functional brain networks that underlie visual working memory in the first two years of life. *Neuroimage, 219*, 116971. doi:https://doi.org/10.1016/j.neuroimage.2020.116971

Ding, X. P., Fu, G., & Lee, K. (2014). Neural correlates of own- and other-race face recognition in children: A functional near-infrared spectroscopy study. *Neuroimage, 85*, 335-344. doi:https://doi.org/10.1016/j.neuroimage.2013.07.051

Douaud, G., Smith, S., Jenkinson, M., Behrens, T., Johansen-Berg, H., Vickers, J., . . . James, A. (2007). Anatomically related grey and white matter abnormalities in adolescent-onset schizophrenia. *Brain, 130*(9), 2375-2386. doi:10.1093/brain/awm184

Emberson, L. L., Crosswhite, S. L., Goodwin, J. R., Berger, A. J., & Aslin, R. N. (2016). Isolating the effects of surface vasculature in infant neuroimaging using short-distance optical channels: a

combination of local and global effects. *Neurophotonics, 3*(3), 031406-031406. doi:10.1117/1.NPh.3.3.031406

Fang, Q. (2010). Mesh-based Monte Carlo method using fast ray-tracing in Plücker coordinates. *Biomedical Optics Express, 1*(1), 165-175. doi:10.1364/boe.1.000165

Fang, Q., & Boas, D. A. (2009a). Monte Carlo simulation of photon migration in 3D turbid media accelerated by graphics processing units. *Opt Express, 17*(22), 20178-20190. doi:10.1364/oe.17.020178

Fang, Q., & Boas, D. A. (2009b, 28 June-1 July 2009). *Tetrahedral mesh generation from volumetric binary and grayscale images.* Paper presented at the 2009 IEEE International Symposium on Biomedical Imaging: From Nano to Macro.

Fang, Q., & Yan, S. (2019). Graphics processing unit-accelerated mesh-based Monte Carlo photon transport simulations. *Journal of Biomedical Optics, 24*(11), 115002. Retrieved from https://doi.org/10.1117/1.JBO.24.11.115002

Fillmore, P. T., Phillips-Meek, M. C., & Richards, J. E. (2015). Age-specific MRI brain and head templates for healthy adults from 20 through 89 years of age. *Front Aging Neurosci, 7*, 44. doi:10.3389/fnagi.2015.00044

Fillmore, P. T., Richards, J. E., Phillips-Meek, M. C., Cryer, A., & Stevens, M. (2015). Stereotaxic Magnetic Resonance Imaging Brain Atlases for Infants from 3 to 12 Months. *Developmental Neuroscience, 37*(6), 515-532. doi:10.1159/000438749

Fu, X., & Richards, J. E. (2020). Investigating Developmental Changes in Scalp-Cortex Correspondence Using Diffuse Optical Tomography Sensitivity in Infancy. *bioRxiv*.

Fu, X., & Richards, J. E. (under review). Investigating Developmental Changes in Scalp-Cortex Correspondence Using Diffuse Optical Tomography Sensitivity in Infancy.

Fukui, Y., Ajichi, Y., & Okada, E. (2003). Monte Carlo prediction of near-infrared light propagation in realistic adult and neonatal head models. *Applied Optics, 42*(16), 6. Retrieved from https://doi.org/10.1364/AO.42.002881

Gervain, J., Mehler, J., Werker, J. F., Nelson, C. A., Csibra, G., Lloyd-Fox, S., . . . Aslin, R. N. (2011). Near-infrared spectroscopy: A report from the McDonnell infant methodology consortium. *Developmental Cognitive Neuroscience, 1*(1), 22-46. doi:https://doi.org/10.1016/j.dcn.2010.07.004

Gilmore, J. H., Shi, F., Woolson, S. L., Knickmeyer, R. C., Short, S. J., Lin, W., . . . Shen, D. (2011). Longitudinal Development of Cortical and Subcortical Gray Matter from Birth to 2 Years. *Cerebral Cortex, 22*(11), 2478-2485. doi:10.1093/cercor/bhr327

Huppert, T. J., Franceschini, M. A., & Boas, D. A. (2009). Noninvasive Imaging of Cerebral Activation with Diffuse Optical Tomography. In R. D. Frostig (Ed.), *In Vivo Optical Imaging of Brain Function* (2nd ed.). Boca Raton, FL: CRC Press/Taylor & Francis.

Jacques, S. L., & Wang, L. (1995). Monte Carlo Modeling of Light Transport in Tissues. In A. J. Welch & M. J. C. Van Gemert (Eds.), *Optical-Thermal Response of Laser-Irradiated Tissue* (pp. 73-100). Boston, MA: Springer US.

Jenkinson, M., Pechaud, M., & Smith, S. M. (2005). BET2: MR-based estimation of brain, skull and scalp surfaces. *In Eleventh Annual Meeting of the Organization for Human Brain Mapping*.

Jurcak, V., Tsuzuki, D., & Dan, I. (2007). 10/20, 10/10, and 10/5 systems revisited: their validity as relative head-surface-based positioning systems. *Neuroimage, 34*(4), 1600-1611. doi:10.1016/j.neuroimage.2006.09.024

Kumar Reddy, A. N., & Sagar, D. K. (2015). Half-width at half-maximum, full-width at half-maximum analysis for resolution of asymmetrically apodized optical systems with slit apertures. *Pramana, 84*(1), 117-126. doi:10.1007/s12043-014-0828-0

Lloyd-Fox, S., Blasi, A., & Elwell, C. E. (2010). Illuminating the developing brain: The past, present and future of functional near infrared spectroscopy. *Neuroscience & Biobehavioral Reviews, 34*(3), 269-284. doi:https://doi.org/10.1016/j.neubiorev.2009.07.008

Makropoulos, A., Aljabar, P., Wright, R., Hüning, B., Merchant, N., Arichi, T., . . . Rueckert, D. (2016). Regional growth and atlasing of the developing human brain. *Neuroimage, 125*, 456-478. doi:https://doi.org/10.1016/j.neuroimage.2015.10.047

Mansouri, C., L'Huillier, J.-p., Kashou, N. H., & Humeau, A. (2010). Depth sensitivity analysis of functional near-infrared spectroscopy measurement using three-dimensional Monte Carlo modeling-based magnetic resonance imaging. *Lasers in Medical Science, 25*(3), 431-438. doi:http://dx.doi.org/10.1007/s10103-010-0754-4

Perdue, K. L., Fang, Q., & Diamond, S. G. (2012). Quantitative assessment of diffuse optical tomography sensitivity to the cerebral cortex using a whole-head probe. *Physics in medicine and biology, 57*(10), 2857. doi:10.1088/0031-9155/57/10/2857

Perdue, K. L., Jensen, S. K. G., Kumar, S., Richards, J. E., Kakon, S. H., Haque, R., . . . Nelson, C. A. (2019). Using functional near-infrared spectroscopy to assess social information processing in poor urban Bangladeshi infants and toddlers. *Developmental Science, 22*(5). doi:10.1111/desc.12839

Perlman, S. B., Luna, B., Hein, T. C., & Huppert, T. J. (2014). fNIRS evidence of prefrontal regulation of frustration in early childhood. *Neuroimage, 85*, 326-334. doi:https://doi.org/10.1016/j.neuroimage.2013.04.057

Pinti, P., Tachtsidis, I., Hamilton, A., Hirsch, J., Aichelburg, C., Gilbert, S., & Burgess, P. W. (2020). The present and future use of functional near-infrared spectroscopy (fNIRS) for cognitive neuroscience. *Annals of the New York Academy of Sciences, 1464*(1), 5-29. doi:10.1111/nyas.13948

Richards, J. E. (in prep). Updating the Neurodevelopmental MRI Database.

Richards, J. E., Boswell, C., Stevens, M., & Vendemia, J. M. (2015). Evaluating methods for constructing average high-density electrode positions. *Brain Topogr, 28*(1), 70-86. doi:10.1007/s10548-014-0400-8

Richards, J. E., & Conte, S. (2020). Brain development in infants: Structure and experience. In C. Tamis-LeMonda & J. J. Lockman (Eds.), *Cambridge Handbook of Infant Development*. Cambridge: Cambridge.

Richards, J. E., Sanchez, C. E., Phillips-Meek, M. C., & Xie, W. (2015). A database of age-appropriate average MRI templates. *Neuroimage, 124*(Pt B), 1254-1259. doi:10.1016/j.neuroimage.2015.04.055

Richards, J. E., & Xie, W. (2015). Brains for all the ages: Structural neurodevelopment in infants and children from a life-span perspective. In J. Bensen (Ed.), *Advances in Child Development and Beahvior* (Vol. 48).

Rorden, C. (2012). MRIcroGL. *Retrieved from McCausland Center: http://www.mccauslandcenter.sc.edu/mricrogl/*.

Rorden, C., & Brett, M. (2000). Stereotaxic Display of Brain Lesions. *Behavioural Neurology, 12*, 421719. doi:10.1155/2000/421719

Sanchez, C. E., Richards, J. E., & Almli, C. R. (2012a). Age-Specific MRI Templates for Pediatric Neuroimaging. *Developmental Neuropsychology, 37*(5), 379-399. doi:10.1080/87565641.2012.688900

Sanchez, C. E., Richards, J. E., & Almli, C. R. (2012b). Neurodevelopmental MRI brain templates for children from 2 weeks to 4 years of age (vol 54, pg 77, 2012). *Developmental Psychobiology, 54*(4), 474-474. doi:10.1002/dev.21018

Schweiger, M., & Arridge, S. (2014). The Toast++ software suite for forward and inverse modeling in optical tomography. *Journal of Biomedical Optics, 19*(4), 040801. Retrieved from https://doi.org/10.1117/1.JBO.19.4.040801

https://www.spiedigitallibrary.org/journals/Journal-of-Biomedical-Optics/volume-19/issue-4/040801/The-Toast-software-suite-for-forward-and-inverse-modeling-in/10.1117/1.JBO.19.4.040801.pdf

Smith, S. M., Jenkinson, M., Woolrich, M. W., Beckmann, C. F., Behrens, T. E. J., Johansen-Berg, H., . . . Matthews, P. M. (2004). Advances in functional and structural MR image analysis and implementation as FSL. *Neuroimage, 23*, S208-S219. doi:https://doi.org/10.1016/j.neuroimage.2004.07.051

Strangman, G., Franceschini, M. A., & Boas, D. A. (2003). Factors affecting the accuracy of near-infrared spectroscopy concentration calculations for focal changes in oxygenation parameters. *Neuroimage, 18*(4), 865-879. doi:10.1016/s1053-8119(03)00021-1

Strangman, G., Li, Z., & Zhang, Q. (2013). Depth Sensitivity and Source-Detector Separations for Near Infrared Spectroscopy Based on the Colin27 Brain Template. *PLOS ONE, 8*(8), e66319. doi:10.1371/journal.pone.0066319

Strangman, G., Zhang, Q., & Li, Z. (2014). Scalp and skull influence on near infrared photon propagation in the Colin27 brain template. *Neuroimage, 85*, 136-149. doi:https://doi.org/10.1016/j.neuroimage.2013.04.090

Tustison, N. J., Avants, B. B., Cook, P. A., Zheng, Y., Egan, A., Yushkevich, P. A., & Gee, J. C. (2010). N4ITK: Improved N3 Bias Correction. *IEEE Transactions on Medical Imaging, 29*(6), 1310-1320. doi:10.1109/tmi.2010.2046908

Wang, Ayaz, H., & Izzetoglu, M. (2019). Investigation of the source-detector separation in near infrared spectroscopy for healthy and clinical applications. *Journal of Biophotonics, 12*(11), e201900175. doi:10.1002/jbio.201900175

Wang, L., Jacques, S. L., & Zheng, L. (1995). MCML—Monte Carlo modeling of light transport in multi-layered tissues. *Computer Methods and Programs in Biomedicine, 47*(2), 131-146. doi:https://doi.org/10.1016/0169-2607(95)01640-F

Whiteman, A., Santosa, H., Chen, D., Perlman, S., & Huppert, T. (2017). Investigation of the sensitivity of functional near-infrared spectroscopy brain imaging to anatomical variations in 5- to 11-year-old children. *Neurophotonics, 5*(1), 011009. Retrieved from https://doi.org/10.1117/1.NPh.5.1.011009

https://www.ncbi.nlm.nih.gov/pmc/articles/PMC5601503/pdf/NPh-005-011009.pdf

Wijeakumar, S., Kumar, A., Delgado Reyes, L. M., Tiwari, M., & Spencer, J. P. (2019). Early adversity in rural India impacts the brain networks underlying visual working memory. *Developmental Science, 22*(5), e12822. doi:10.1111/desc.12822

Yan, S., Tran, A. P., & Fang, Q. (2019). Dual-grid mesh-based Monte Carlo algorithm for efficient photon transport simulations in complex three-dimensional media. *Journal of Biomedical Optics, 24*(2), 020503. Retrieved from https://doi.org/10.1117/1.JBO.24.2.020503

Yaroslavsky, A. N., Schulze, P. C., Yaroslavsky, I. V., Schober, R., Ulrich, F., & Schwarzmaier, H. J. (2002). Optical properties of selected native and coagulated human brain tissues in vitro in the visible and near infrared spectral range. *Phys Med Biol, 47*(12), 2059-2073. Retrieved from https://www.ncbi.nlm.nih.gov/pubmed/12118601

Zimeo Morais, G. A., Balardin, J. B., & Sato, J. R. (2018). fNIRS Optodes' Location Decider (fOLD): a toolbox for probe arrangement guided by brain regions-of-interest. *Scientific Reports, 8*(1), 3341. doi:10.1038/s41598-018-21716-z

Supplemental Materials

Table 1: References of optical properties used in published studies.

Table 2: Source-detector separation information for “all electrode pairs” constructed from 10-5 electrode locations.

It provides the minimum and maximum distances specified for each target separation distance (10mm to 60mm in 5mm increment) for all age groups.

Figure 1: Mean numbers of nodes and elements for the dense and sparse finite element model (FEM) mesh by age group.

Figure 2: Mean number of source-detector channels selected for the target separation distances by age group.

Figure 3: Examples of S-D Channel DOT fluence sensitivity profile by channel from an individual subject in each age group at 20mm and 50mm separations.

Figure 4: Variance of S-D Channel DOT fluence sensitivity profile by age at 30mm and 50mm separations.